ACS APPLIED MATERIALS & INTERFACES

www.acsami.org

Research Article

Nucleus-Targeting Manganese Dioxide Nanoparticles Coated with the Human Umbilical Cord Mesenchymal Stem Cell Membrane for Cancer Cell Therapy

Lixu Xie, Changwen Zhang, Miao Liu, Jianling Huang, Xiao Jin, Changjun Zhu, Minjie Lv, Ning Yang, Sixi Chen, Mingyue Shao, Xingran Du, and Ganzhu Feng*

Cite This: *ACS Appl. Mater. Interfaces* 2023, 15, 10541−10553

Read Online

ACCESS | Metrics & More | Article Recommendations | Supporting Information

ABSTRACT: Recently, development of drug delivery systems for accurate delivery of antitumor drugs to tumor sites to improve their antitumor efficacy has attracted great interest in the area of cancer immunotherapy. In this report, an intelligent biodegradable hollow manganese dioxide ($HMnO_2$) nanoparticle (NP) with a human umbilical cord mesenchymal stem cell (hUC-MSC) membrane coating was designed to exert efficient chemo-immunotherapy for cancer treatment. A TAT peptide-modified membrane structure was constructed for nuclear targeting. Our findings showed that this new nanoreactor inherited the active targeting capability of MSCs and exhibited tumoritropic accumulation significantly at the cancerous parts. Compared with other formulations, intravenous injection of the NPs markedly inhibited tumor growth, relapse, and metastasis. Moreover, we found that the NPs effectively boosted dendritic cell maturation and recruited effector T cells into tumors. Overall, this work demonstrates the great potential of applying MSC membrane-coated manganese dioxide NPs as nucleus-targeting nanocarriers in cancer chemo-immunotherapy.

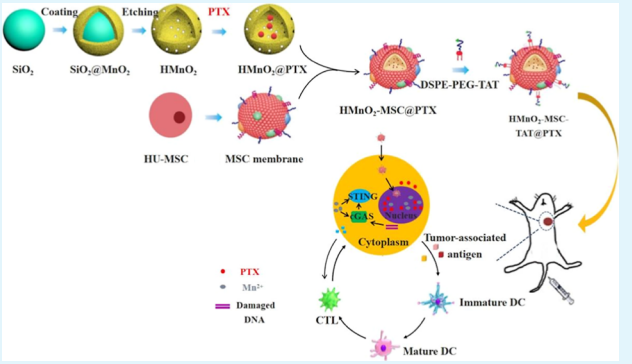

KEYWORDS: *biomimetic delivery platforms, tumor immunotherapy, mesenchymal stem cell, manganese dioxide, nuclear-targeted*

INTRODUCTION

Lung cancer is the second most commonly diagnosed cancer and the leading cause of cancer death.[1] The 5 year survival rate of lung cancer is presently less than 20%.[2] A combination of paclitaxel (PTX), a traditional anticancer drug and platinum drugs, is the first-line chemotherapy for multiple solid tumors.[3] However, the low concentration of PTX at the tumor sites not only attenuates the therapeutic outcome but also augments the toxicity to normal tissues. The tumor microenvironment not only plays an important role during tumor initiation, progression, and metastasis but also heavily abates the efficacy in many conventional treatment strategies.[4] To enhance the drug concentration in the tumor microenvironment, there is an urgent need to deliver PTX efficiently and precisely to target tissues and eradicate tumor cells.

Over the last decades, nanomedicine has shown great promise and made breakthrough progress in the fields of cancer diagnosis and treatment.[5] However, most drug delivery systems are based on "passive" delivery vehicles, which rely on the enhanced permeability and retention effect of affected vasculature to accumulate drugs in tumor sites.[6] Unfortunately, due to the lack of an active tumor-targeting mechanism and the limited ability to escape immune surveillance, such passive carriers are considered insufficient to achieve efficient drug delivery in vivo.[7] To confer tumor-targeting capability, many strategies have been explored, including modification with tumor-specific ligands (e.g., folic acid,[8] peptides,[9] and antibodies[10]). However, these chemically modified "active" drug-loaded carrier particles can easily activate the reticuloendothelial system (RES) and are still cleaned out.[11] Consequently, an ideal tumor-targeting drug delivery system must incorporate an ability to target tumors, avoid clearance, and overcome vascular barriers for enhanced in vivo tumor therapy.

Recently, natural cells, such as erythrocytes,[12] dendritic cells (DCs),[13] mesenchymal stem cells (MSCs),[14] and macrophages,[15] have been explored as drug carriers. For example, erythrocytes are an attractive first choice for designing diverse biomimetic camouflage strategies, owing to their superior blood circulation half-life and limited immune cell clearance.

Received: January 26, 2023
Accepted: February 3, 2023
Published: February 14, 2023

Scheme 1. Preparation of $HMnO_2$-MSC-TAT NPs and Schematic Illustration of Chemo-immunotherapy

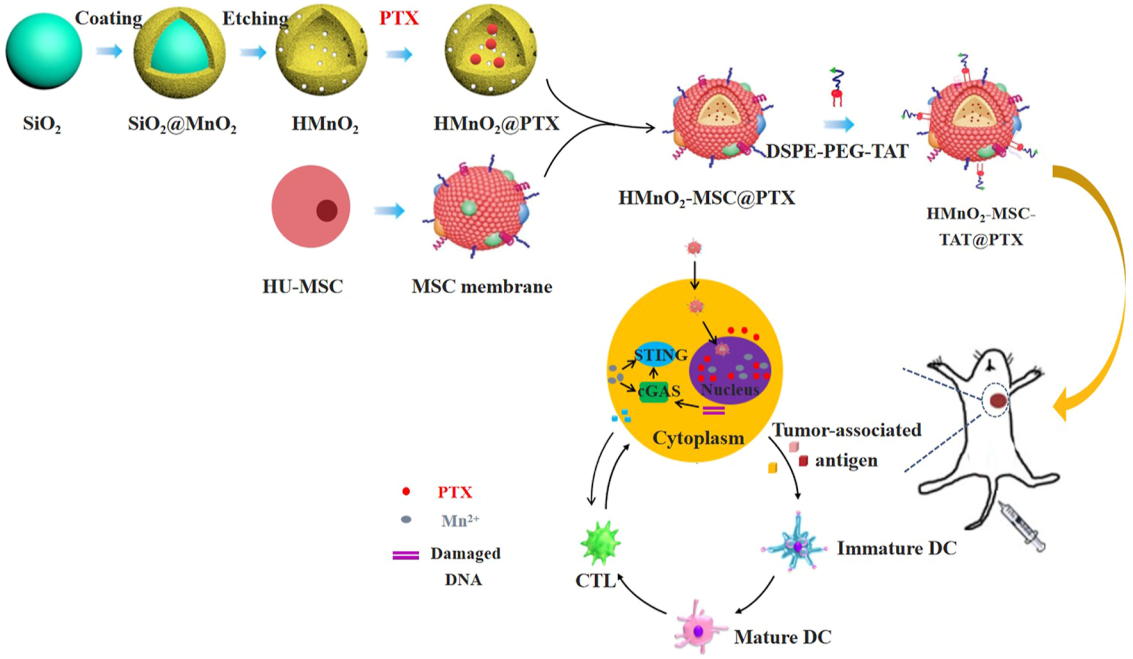

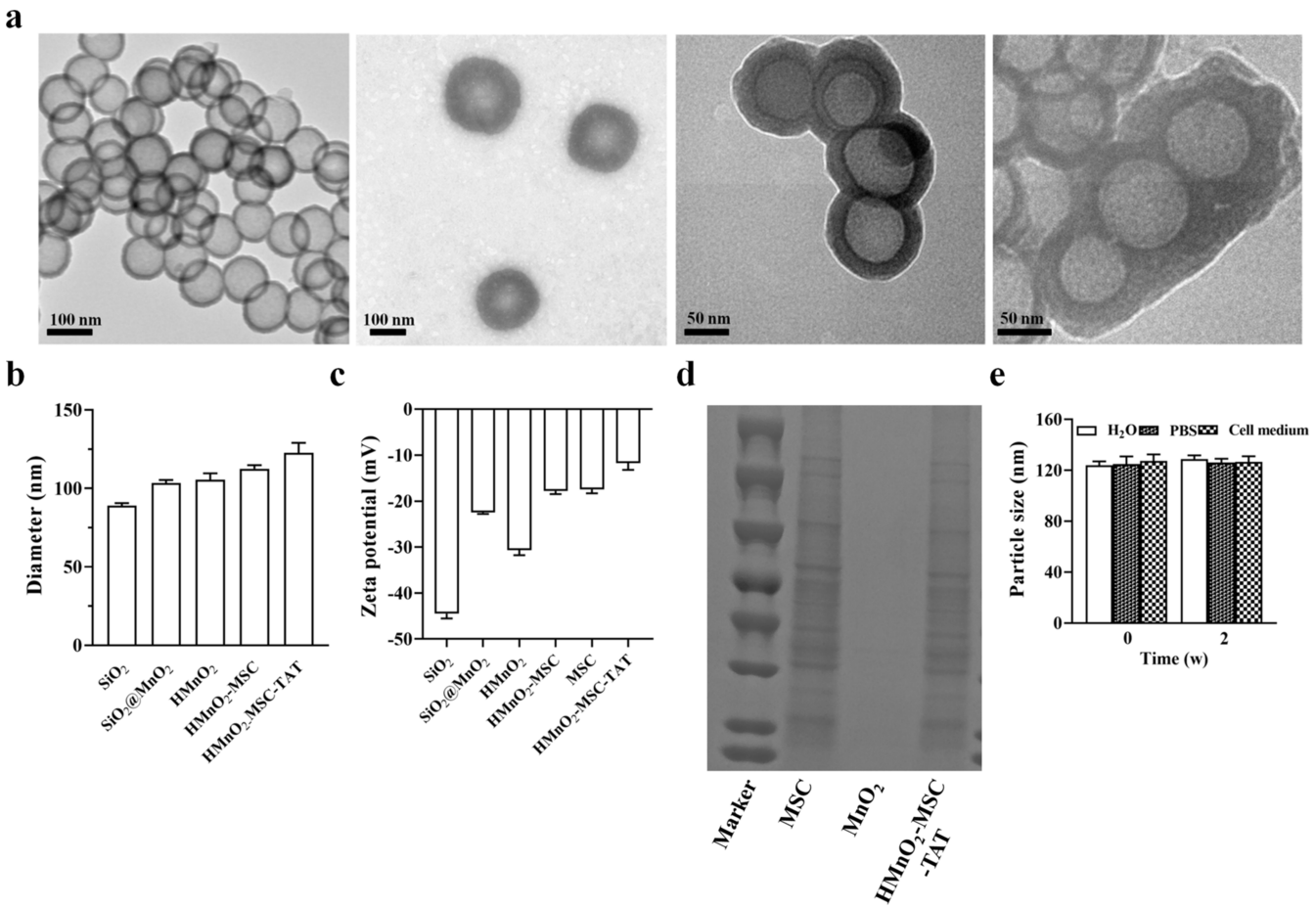

Figure 1. Synthesis and characterization of NPs. (a) TEM images of $HMnO_2$ NPs, MSC membranes, $HMnO_2$-MSC NPs, and $HMnO_2$-MSC-TAT NPs. (b) Hydrodynamic sizes and (c) surface charges of SiO_2 NPs, SiO_2@MnO_2 NPs, $HMnO_2$ NPs, $HMnO_2$-MSC NPs, and $HMnO_2$-MSC-TAT NP samples measured by DLS. Data are presented as the mean ± SD (n = 3). (d) Protein profiles of the MSC membrane, $HMnO_2$ NPs, and $HMnO_2$-MSC-TAT NPs were analyzed by SDS-PAGE. (e) In vitro stability of $HMnO_2$-MSC-TAT NPs maintained in H_2O, PBS, and cell culture medium at 4 °C for 2 weeks. Data are presented as the mean ± SD (n = 3).

https://doi.org/10.1021/acsami.3c01176
ACS Appl. Mater. Interfaces 2023, 15, 10541−10553

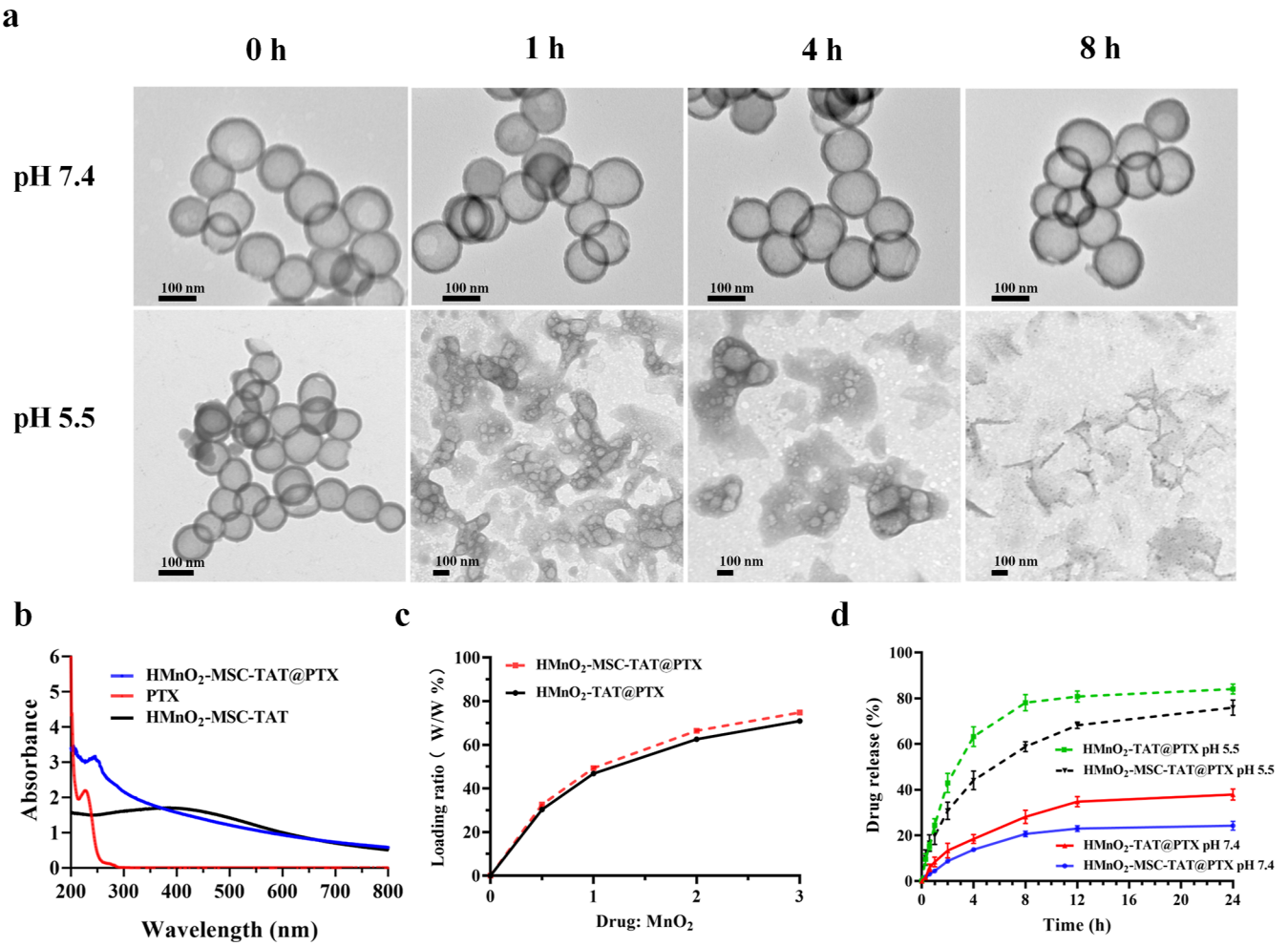

Figure 2. pH-dependent NP decomposition and drug behaviors. (a) TEM images of $HMnO_2$ NPs after incubation in buffers with different pH values (7.4 and 5.5) for various periods of time. (b) UV−vis spectra of free PTX, $HMnO_2$-MSC-TAT NPs, and $HMnO_2$-MSC-TAT@PTX NPs. (c) PTX loading weight ratios of $HMnO_2$-TAT NPs and $HMnO_2$-MSC-TAT NPs at various ratios of feeding drug: MnO_2. Data are presented as the mean ± SD (n = 3). (d) In vitro cumulative release profiles of PTX released from $HMnO_2$-TAT NPs or $HMnO_2$-MSC-TAT NPs in PBS at pH 7.4 and 5.5. Data are presented as the mean ± SD (n = 3).

However, erythrocyte membranes lack relevant targeting ligands to cancer cells and thus limit their applications. MSC-based drug delivery systems have shown considerable capabilities, such as inherent tumor-tropic properties, long circulation times, and hypoimmunogenicity.[14,16,17] However, some researchers have confirmed that mesenchymal stem cells may promote tumor progress or even differentiate into tumors.[18−20] Moreover, some concerning results indicate that whole cell-based drug carriers may be potentially contaminated with biological materials and have biosafety problems.[21] In order to overcome these disadvantages, researchers have strove to eliminate the nucleic matters and developed novel cell membrane-coated particles with minimum membrane protein loss.[22−24] Such cell membrane-camouflaged nanoparticles (NPs) inherit various biological functions and/or targeting specificities of natural cells. Multiple cell membranes, including erythrocytes,[25,26] white blood cells,[27,28] stem cells,[29,30] and platelets,[31,32] have been utilized to develop biomimetic NPs, which possess many desirable properties.

The construction of drug carriers based on human umbilical cord-derived mesenchymal stem cell (hUC-MSC) membrane-cloaked NPs has never been reported until recently reported by the Yang group.[33] However, they did not design the cell membrane-camouflaged NPs for targeting the cell nucleus. Herein, we developed hUC-MSC membrane-coated hollow manganese dioxide ($HMnO_2$) with TAT peptide modification as a high-performance nucleus-targeting drug delivery system. Because the intact MSC membrane surface proteins maintained the tumor homing properties and TAT peptide promoted nuclear localization,[34] our $HMnO_2$-MSC-TAT@PTX efficiently targeted the nucleus in vitro; moreover, upon intravenous injection, this novel carrier effectively targeted tumors and significantly enhanced the drug concentration in the tumor. Due to the synergetic antitumor effect of PTX, which induces immunogenic cell death (ICD), and Mn^{2+}, which augments cyclic GMP-AMP synthase (cCAS) and stimulator of interferon genes (STING) activation,[35,36] $HMnO_2$-MSC-TAT@PTX promoted DC maturation and effector T cell infiltration, and thus, these properties are beneficial for lung cancer treatment. The detailed synthetic procedures and treatment processes are illustrated in Scheme 1.

RESULTS AND DISCUSSION

Preparation and Characterization of $HMnO_2$-MSC-TAT NPs. $HMnO_2$ NPs were synthesized via a three-step

https://doi.org/10.1021/acsami.3c01176
ACS Appl. Mater. Interfaces 2023, 15, 10541−10553

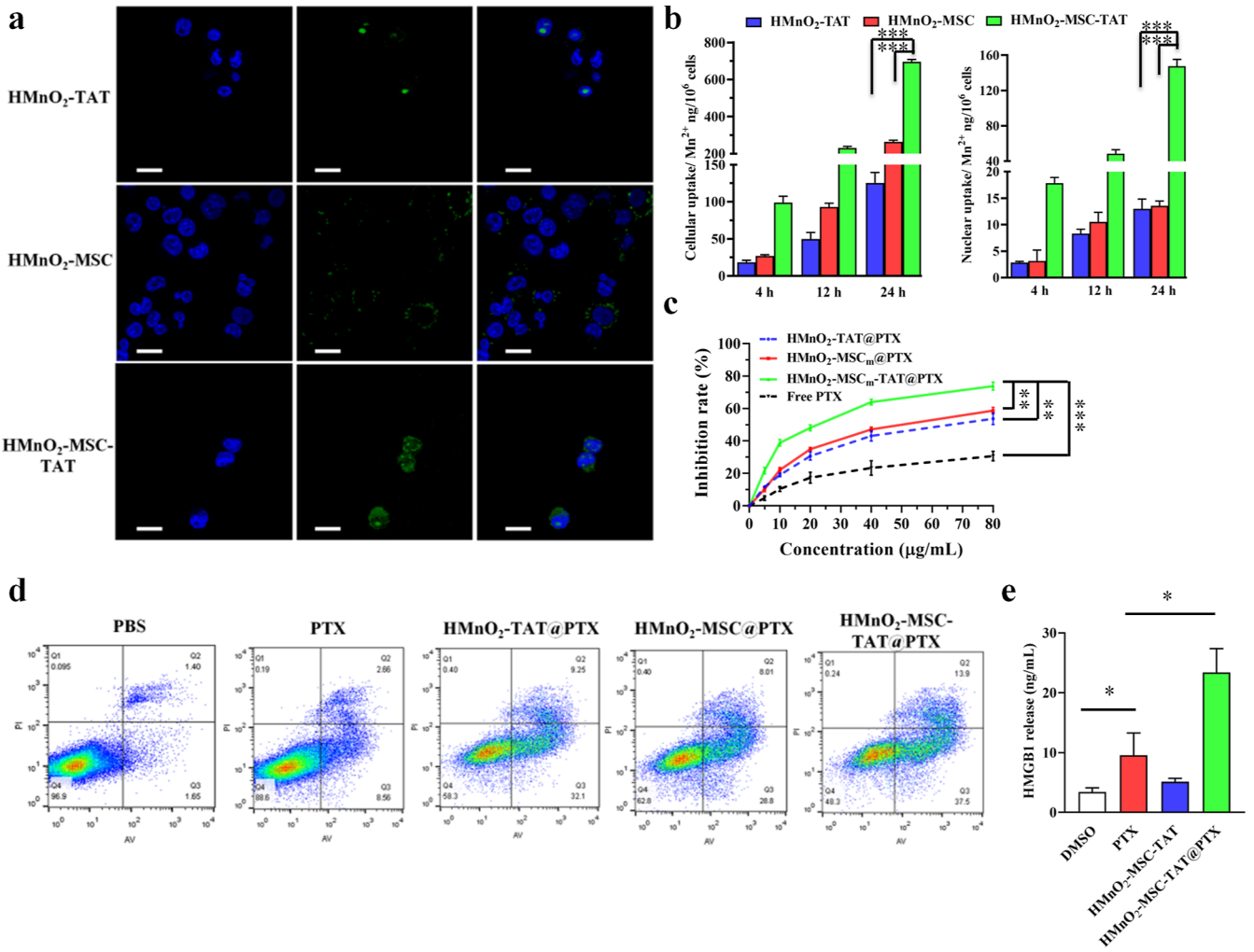

Figure 3. Cellular and nuclear uptake and antitumor activity of nanoparticles in vitro. (a) CLSM images of A549 cells incubated with FITC-loaded $HMnO_2$-TAT NPs, $HMnO_2$-MSC NPs, or $HMnO_2$-MSC-TAT NPs. The scale bar is 50 μm. For each panel, the images from left to right show cell nuclei stained by DAPI (blue), FITC fluorescence from NP in cells (green), and overlays of the two images. (b) Amount of cellular and nuclear uptake of NPs by A549 cells at different time points. Data are presented as the mean ± SD (n = 3), and statistical significance was calculated using Student's t test (***p < 0.001). (c) Inhibition of A549 cells after 24 h incubation with free PTX, $HMnO_2$-TAT@PTX NPs, $HMnO_2$-MSC@PTX NPs, or $HMnO_2$-MSC-TAT@PTX NPs. Data are presented as the mean ± SD (n = 3), and statistical significance was calculated using Student's t test (**p < 0.01 and ***p < 0.001). (d) Apoptosis rates were assessed by flow cytometry (upper right quadrant and lower right quadrant represent apoptotic cells). (e) Amount of released HMGB1. Data are presented as the mean ± SD (n = 3), and statistical significance was calculated using Student's t test (*p < 0.05 and **p < 0.01).

reaction[37] (Figure S1). MSC membrane-cloaked NPs were fabricated by coextruding the MSC membrane fragments and $HMnO_2$ NP cores.[22] To further modify with TAT, the prepared membrane-cloaked NPs were incubated with TAT-conjugated 1,2-distearoyl-*sn*-glycero-3-phosphoethanolamine-*N*-methoxy (polyethylene glycol) (DSPE-PEG-TAT), whose carbon−hydrogen chains were spontaneously incorporated onto cell membranes using a lipid-insertion approach.[39]

The transmission electron microscopy (TEM) image of $HMnO_2$ in Figure 1a clearly shows a regularly spherical and hollow structure with diameter of ∼80 nm, which could also be found in scanning electron microscopy (SEM) images (Figure S2). The surface of $HMnO_2$ was encapsulated with MSC membrane to obtain $HMnO_2$-MSC. As revealed by TEM, a lipid layer could be clearly seen on the surface of $HMnO_2$ (Figure 1a), demonstrating the successful coating with the cell membrane. As measured by dynamic light scattering (DLS), the hydrodynamic size of the resulting membrane-cloaked NPs was increased from 107.4 ± 7.3 nm to 116.5 ± 5.7 nm upon coating with MSCs (Figure 1b). DLS measurements indicated successfully being coated with MSC membranes as the size of $HMnO_2$ NPs increased to closely that of pure membrane. The zeta potential changed from −30.6 ± 1.1 mV (uncoated NPs) to −17.8 ± 0.6 mV (MSC membrane-coated NPs), which was approximate to that of MSC membranes (−17.4 ± 0.9 mV) (Figure 1c). TAT peptide was conjugated to the outer surface of $HMnO_2$-MSC, which showed the peak corresponding to TAT at 490 nm by UV−vis absorbance spectrometry (Supporting Information, Figure S3). The average hydrodynamic size of $HMnO_2$-MSC-TAT NPs increased to 124.3 ± 4.9 nm (Figure 1b), probably due to the additional PEG chains incorporated onto MSC membranes after $HMnO_2$-MSCs were modified by DSPE-PEG-TAT. Subsequently, the membrane protein ingredients of $HMnO_2$-MSC-TAT were detected by sodium dodecyl sulfate polyacrylamide gel electrophoresis (SDS-PAGE). The PAGE protein separation assay showed that

https://doi.org/10.1021/acsami.3c01176
ACS Appl. Mater. Interfaces 2023, 15, 10541−10553

the protein was undetectable in bare NPs, significant and similar amounts of protein were detected in natural cell membranes and $HMnO_2$-MSC-TAT samples (Figure 1d). TEM images showed that $HMnO_2$-TAT NPs was a characteristic core−shell structure, and the zeta potential of $HMnO_2$-TAT NPs was 21.9 ± 3.4 mV (Figure S4).

To further text for the long-term stability of the $HMnO_2$-MSC-TAT NPs, they were suspended in three commonly used biological media, that is, distilled water, pH 7.4 phosphate buffer solution (PBS), and cell culture medium. The NP size was continuously monitored by DLS for 2 weeks. The minimal changes of size confirmed the good stability of $HMnO_2$-MSC-TAT NPs in stock solution (Figure 1e).

To evaluate the safety of $HMnO_2$-MSC-TAT NPs to cells, we determined the viability of LO2 cells and BEAS-2B cells using the MTT assay (Figure S5). Even when the NP concentration was increased, the cell survival rate remained above 80%, which confirmed the low toxicity of our drug carrier.

pH-Dependent NP Decomposition and Drug Behaviors. The tumor microenvironment responsiveness is the essential property for $HMnO_2$-MSC-TAT to realize drug release at the tumor site. Figure 2a shows $HMnO_2$ NPs dissolved in solutions of different pH (7.4 and 5.5) values for various durations. The morphology of $HMnO_2$ NPs in the pH 7.4 solution after 8 h remained almost intact. In contrast, these pH-responsive hollow particles appeared swollen at pH 5.5 and was then hardly observable after 8 h. To examine the degradation rates of the obtained $HMnO_2$-MSC-TAT NPs, we measured the MnO_2-characteristic absorbance band by UV−vis spectra (Figure S6). The results further demonstrate the ultrasensitive response to the acidic tumor microenvironment.

The surface area and average pore size of $HMnO_2$ were calculated to be 106.24 $m^2\ g^{-1}$ and 8 nm, respectively, by the Brunauer−Emmett−Teller (BET) method (Figure S7). The hollow structures of $HMnO_2$ were utilized for efficient drug loading. To prepare PTX-loaded nanoshells, those nanoshells were mixed with different concentrations of PTX under overnight stirring. UV−vis spectra of $HMnO_2$-MSC-TAT@PTX showed the absorption peak of PTX at 227 nm, demonstrating that PTX was successfully loaded (Figure 2b). At the proportion (PTX/MnO_2) of 3:1, the PTX loading efficiency of $HMnO_2$-MSC-TAT and $HMnO_2$-TAT reached rather high ratios of 74.9 and 70.91%, respectively (Figure 2c).

To mimic the drug release behaviors of $HMnO_2$-TAT@PTX and $HMnO_2$-MSC-TAT@PTX NPs in physiological states, the release profile was evaluated by dialyzing NPs at pH 7.4 and pH 5.5 (Figure 2d). At pH 7.4, about 37.9% of PTX was released from $HMnO_2$-TAT@PTX after 24 h. However, only 24.3% of PTX was released from $HMnO_2$-MSC-TAT@PTX, which indicated that MSC membranes may play the part of protective layer and hinder the leakage of PTX from the $HMnO_2$-TAT@PTX NPs. When tested at pH 5.5, 84.1 and 76.1% of PTX were released from $HMnO_2$-TAT@PTX and $HMnO_2$-MSC-TAT@PTX within 24 h, respectively. Moreover, $HMnO_2$-MSC-TAT released PTX more slowly compared with $HMnO_2$-TAT@PTX, which may be caused by the MSC barriers. These results indicated that $HMnO_2$-MSC-TAT@PTX NPs had advantaged in improving the drug-loading capacity and controlling the drug release behavior.

Cellular Uptake Results In Vitro. To understand the cellular and nuclear uptakes of $HMnO_2$-MSC-TAT NPs, A549 cells were incubated with $HMnO_2$-TAT NPs, $HMnO_2$-MSC NPs, and $HMnO_2$-MSC-TAT NPs (100 μg/mL) for 12 h and then imaged by confocal laser scanning microscopy (CLSM). To visualize the location of $HMnO_2$ NPs at the subcellular level, FITC-labeled $HMnO_2$-MSC-TAT NPs were synthetized in a similar way as $HMnO_2$-MSC-TAT@PTX NPs. In the absence of MSC membranes, a weak green fluorescence signal could be found in the cytoplasm, indicating that $HMnO_2$-TAT NPs could hardly be taken up into the cells (Figure 3a). In contrast, $HMnO_2$-MSC NPs could enter the cells much more efficiently due to the inherent tumor-tropic property of MSCs, as demonstrated by a significant enhancement of the green fluorescence signal from $HMnO_2$-MSC NPs in the cytoplasm (Figure 3a). Importantly, the green fluorescence signal in the nuclear region indicated that $HMnO_2$-MSC-TAT NPs successfully penetrated into nuclei (Figure 3a). This proves that the TAT peptide plays a crucial role in the nucleus targeting process.

The quantification of cellular and nuclear uptakes of NPs (Figure 3b), determined by ICP-OES measurements of the Mn contents, further demonstrated that $HMnO_2$-MSC-TAT NPs could specifically target A549 cells, thanks to the MSC membranes, resulting in remarkably enhanced cellular uptake (5.6 times that of $HMnO_2$-TAT NPs). Furthermore, $HMnO_2$-MSC-TAT NPs greatly promoted nuclear penetration (11.3 times that of $HMnO_2$-MSC NPs).

In Vitro Cytotoxicity Evaluation and Anticancer Effects. To study the anticancer effect of NPs, we incubated A549 cells with different preparations. The blank $HMnO_2$-TAT NPs, $HMnO_2$-MSC NPs, and $HMnO_2$-MSC-TAT NPs had little effect on the viability of A549 cells (Supporting Information, Figure S8). When cells were treated with $HMnO_2$-MSC-TAT@PTX NPs for 24 h, cell viability was lower than those treated with $HMnO_2$-TAT@PTX NPs, $HMnO_2$-MSC@PTX NPs, or free PTX at the same dose (Figure 3c).

As shown in Figure 3d, the cellular apoptosis rates were 11.0, 33.3, 35.7, and 51.7% when treated with free PTX, $HMnO_2$-TAT@PTX, $HMnO_2$-MSC@PTX, and $HMnO_2$-MSC-TAT@PTX, respectively. These results indicate that this drug delivery system induced higher cellular apoptosis than free PTX. Moreover, the cytotoxicity of $HMnO_2$-MSC-TAT@PTX against cancer cells is remarkably higher than that of either $HMnO_2$-TAT@PTX or $HMnO_2$-MSC@PTX due to the specific targeting effect of MSC membranes and nuclear targeting of TAT peptides.

In Vitro Induction of High Mobility Group Box 1 (HMGB1) Release. Recent studies have shown that PTX can elicit ICD by triggering apoptotic tumor cells to secrete damage-associated molecular patterns (DAMPs), such as calreticulin expression and HMGB1 release.[40,41] Next, to study whether $HMnO_2$-MSC-TAT@PTX can induce ICD, the levels of HMGB1 were examined. Compared with the control, the samples treated with PTX or $HMnO_2$-MSC-TAT@PTX NPs showed significantly increased HMGB1 release (Figure 3e). It was also found that $HMnO_2$-MSC-TAT@PTX NPs induced a comparatively greater release of HMGB1 than PTX. This demonstrated that $HMnO_2$-MSC-TAT@PTX could enhance the ICD response in vitro.

Biodistribution and Pharmacokinetics Study of $HMnO_2$-MSC-TAT NPs. To monitor the in vivo distribution of NPs, a near-infrared fluorescent dye, ICG, was loaded into $HMnO_2$-TAT@ICG NPs, $HMnO_2$-MSC@ICG NPs, and

https://doi.org/10.1021/acsami.3c01176
ACS Appl. Mater. Interfaces 2023, 15, 10541−10553

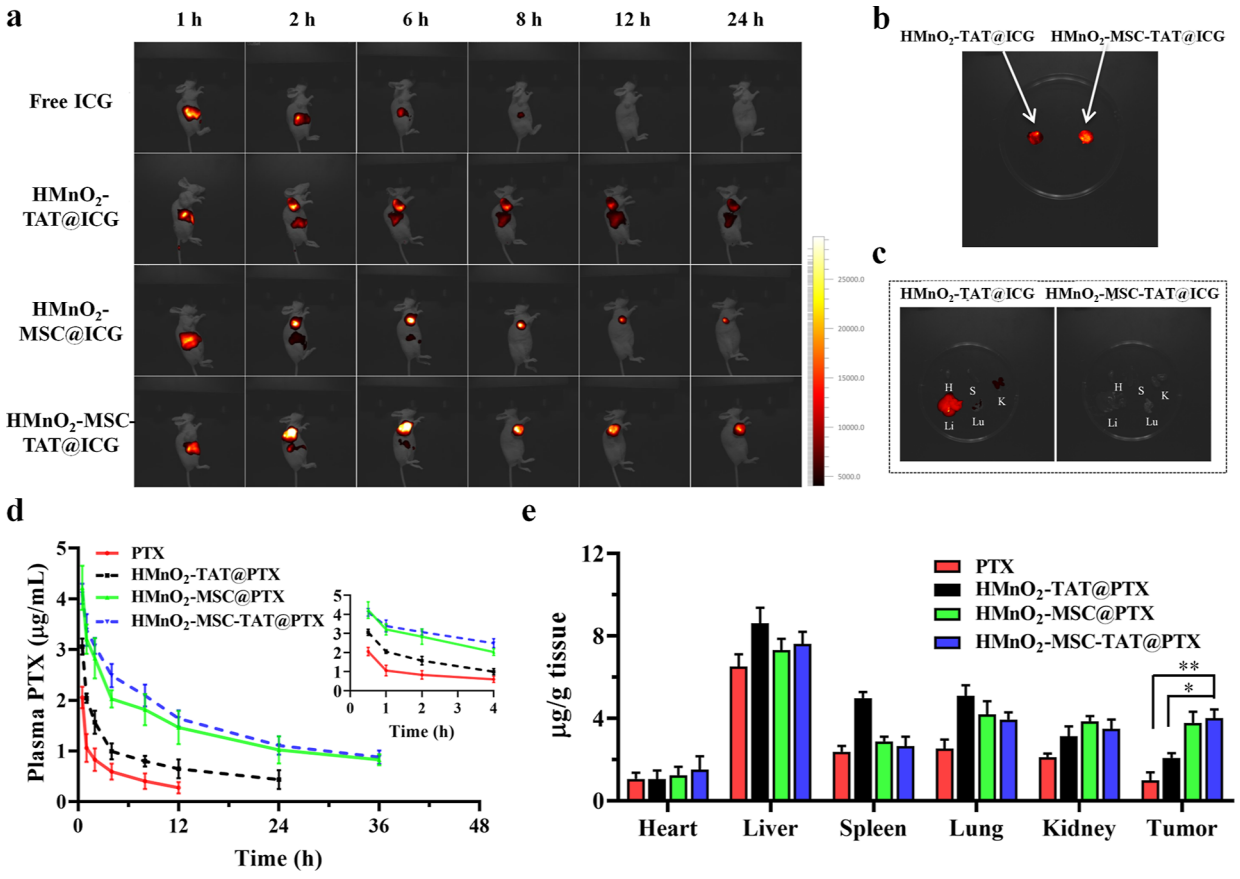

Figure 4. Biodistribution and pharmacokinetics study of $HMnO_2$-MSC-TAT NPs. (a) In vivo imaging of A549 tumor-bearing mice at different time points after intravenous administration of free ICG, $HMnO_2$-TAT@ICG NPs, $HMnO_2$-MSC@ICG NPs, or $HMnO_2$-MSC-TAT@ICG NPs. (b,c) Ex vivo images of tumors (b) and other tissues (c) 24 h after treatment with the various formulations. (d) Pharmacokinetics of drugs in plasma. (e) In vivo biodistribution of PTX in LLC tumor-bearing C57BL/6 mice at 24 h after i.v. injection of PTX, $HMnO_2$-TAT@PTX NPs, $HMnO_2$-MSC@PTX NPs, or $HMnO_2$-MSC-TAT@PTX NPs at a dosage of 4 mg of PTX/kg. Data are presented as the mean ± SD (n = 3), and statistical significance was calculated using Student's t test (*p < 0.05 and **p < 0.01).

$HMnO_2$-MSC-TAT@ICG NPs. At various time points after injection, the fluorescence signals were monitored by in vivo imaging. As displayed in Figure 4a, free ICG had no significant aggregating in the tumor site 24 h after injection. Notably, the fluorescence of ICG delivered by $HMnO_2$-TAT NPs, $HMnO_2$-MSC NPs, and $HMnO_2$-MSC-TAT NPs peaked at approximately 2, 6, and 6 h, respectively. The fluorescence signal of $HMnO_2$-MSC-TAT@ICG NPs was significantly stronger than that of $HMnO_2$-TAT@ICG NPs, especially at 24 h after injection. To determine the precise localization of NPs, major organs and tumors were collected 24 h after injection. As shown in Figure 4b, the fluorescence intensity in tumors was greater in animals treated with $HMnO_2$-MSC-TAT NPs than that in animals treated with $HMnO_2$-TAT, which further confirmed the tumor-targeting property of $HMnO_2$-MSC-TAT NPs. Altogether, $HMnO_2$-MSC-TAT NPs were able to efficiently target tumor, and the amount of $HMnO_2$-MSC-TAT NPs internalized by the liver and lung was less than that of $HMnO_2$-TAT NPs (Figure 4c), indicating that MSC membrane coating effectively decreased its clearance by RES.

To examine the pharmacokinetics, the plasma PTX concentration was measured after intravenous injections of PTX or PTX nano-carriers (Figure 4d). PTX concentrations at 0.5 h after $HMnO_2$-MSC-TAT@PTX NP injection were 1.99-fold higher than that after PTX injection and 1.34-fold higher than that after $HMnO_2$-TAT@PTX NP injection. PTX became undetectable 12 h after free PTX injection, 24 h after $HMnO_2$-TAT@PTX injection, and 36 h after $HMnO_2$-MSC-TAT@PTX injection. These observations indicate that the circulation time was also evidently prolonged.

Furthermore, the biodistribution of PTX was explored in C57BL/6 tumor-bearing mice (Figure 4e). $HMnO_2$-MSC-TAT@PTX NPs showed significantly more accumulation in tumors compared with that of free PTX or $HMnO_2$-TAT@PTX NPs. At 24 h, PTX concentration in the tumor tissues treated with $HMnO_2$-MSC-TAT@PTX NPs was 4.01 μg/g, which was 4.05-fold that of animals treated with free PTX or 1.93-fold that of $HMnO_2$-TAT@PTX NPs, while there was no significant difference between those treated with $HMnO_2$-MSC-TAT@PTX NPs and $HMnO_2$-MSC@PTX NPs. This phenomenon can be explained by the tumor-tropic property of MSC membranes, which may be conducive for $HMnO_2$-MSC-TAT NPs to exert a better therapeutic effect than $HMnO_2$-TAT. When compared to the NP groups, free PTX showed a slightly faster elimination at all observation time points in the tissue samples (heart, liver, spleen, lungs, and kidneys) (Figure 4e). These results indicate that $HMnO_2$-MSC-TAT efficiently accumulated and remained in tumors after i.v. injection, which could be propitious to anticancer applications in vivo.

In Vivo Antitumor Efficacy. In a tumor growth inhibition assay, a unilateral tumor model was developed according to the scheme shown in Figure 5a. When the tumor sizes approached

https://doi.org/10.1021/acsami.3c01176
ACS Appl. Mater. Interfaces 2023, 15, 10541−10553

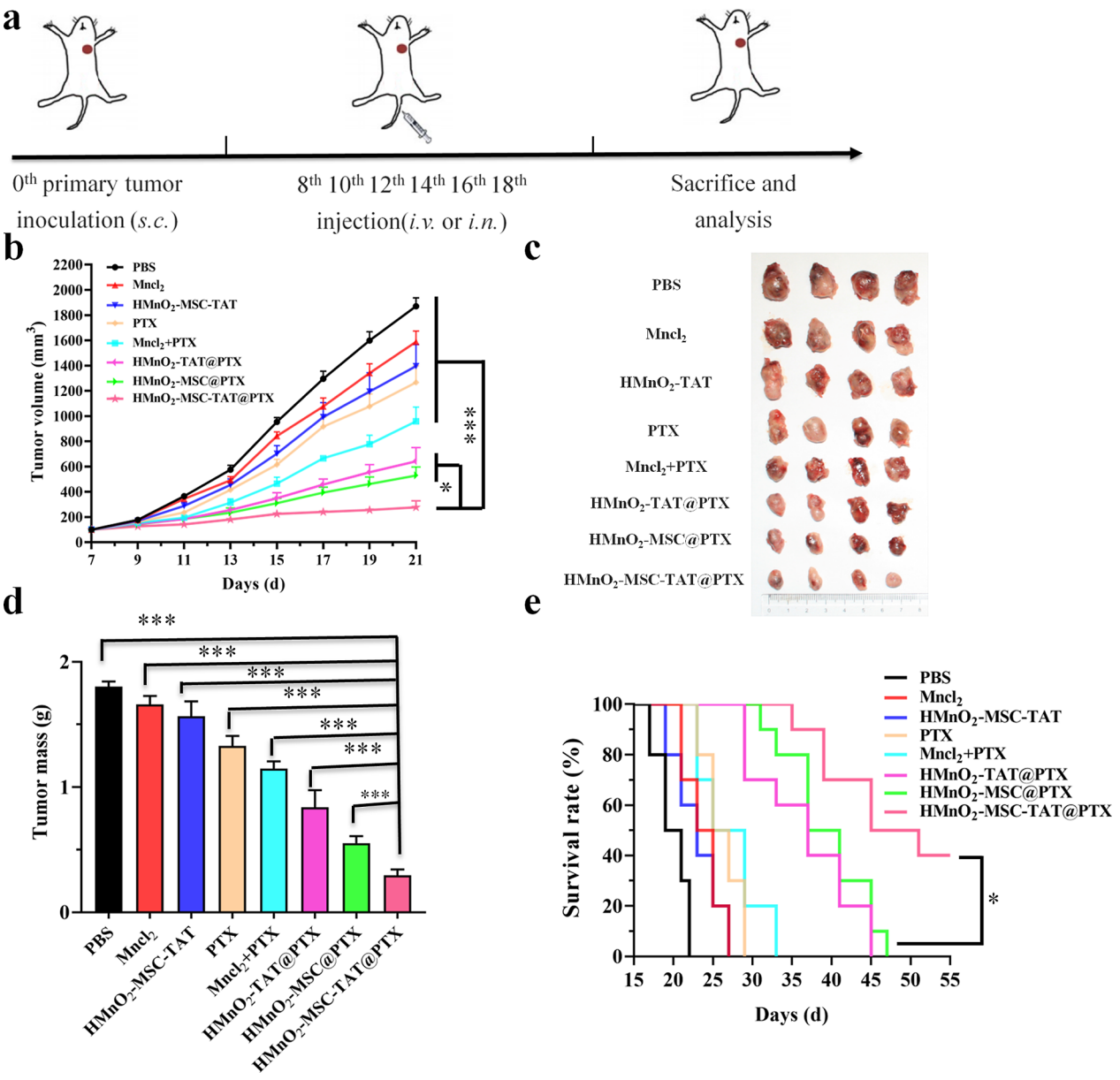

Figure 5. In vivo antitumor efficacy. (a) Schematic illustration of the drug administration schedule. (b) LLC tumor growth curves in mice after i.v. drug administration. Data are presented as the mean ± SD (n = 4), and statistical significance was calculated using Student's t test (*p < 0.05 and ***p < 0.001). (c) Representative images of the excised tumors after various treatments. (d) Tumor weights of each group after 15 d of treatment. (e) Percentages of surviving mice treated with various formulations. Data are presented as the mean ± SD (n = 10).

100 mm^3, tumor-bearing C57BL/6 mice were randomly assigned to eight treatment groups: PBS, $MnCl_2$, $HMnO_2$-MSC-TAT NPs, free PTX, $MnCl_2$ + PTX, $HMnO_2$-TAT@PTX NPs, $HMnO_2$-MSC@PTX NPs, and $HMnO_2$-MSC-TAT@PTX NPs. The tumor sizes were measured for the following 2 weeks. At day 21, the tumors were harvested and weighed.

As illustrated in Figure 5b,c, tumor growth was minimally inhibited in groups treated with $MnCl_2$, $HMnO_2$-MSC-TAT NPs, or free PTX. $MnCl_2$ + free PTX demonstrate an enhanced antitumor efficiency and reduced the tumor size to 51.2% that of PBS treatment at day 21. This may be attributed to the synergetic effects of chemo-immunotherapy. Released PTX could cause dying tumor cells and secrete or exposure of DAMPs. Meanwhile, Mn^{2+} could induce the maturation of DCs and T-cell infiltration through the PTX-triggered cGAS/STING pathway. PTX can induce DNA damage and activate the classical STING/TBK1/IRF3 pathway and non-classical STING-NF-κB signaling complex.[42] In addition to chemotherapeutic agents, manganese can enhance STING activation. Hou et al. designed a manganese-based drug-loaded carrier particles, which could increase the concentration of drug for inducing DNA damage and Mn^{2+} to enlarge STING activity, boosting DC maturation and increasing cytotoxic T lymphocyte (CTL) infiltration in tumor sites.[43] Remarkably, compared with the $HMnO_2$-TAT@PTX NPs (34.3%) and $HMnO_2$-MSC@PTX NPs (28.2%), tumor growth was more effectively inhibited in the $HMnO_2$-MSC-TAT@PTX group (14.8% tumor size of PBS) at day 21. Similarly, the superior antitumor effect of $HMnO_2$-MSC@PTX NPs was also proved by tumor weighting (Figure 5d).

https://doi.org/10.1021/acsami.3c01176
ACS Appl. Mater. Interfaces 2023, 15, 10541−10553

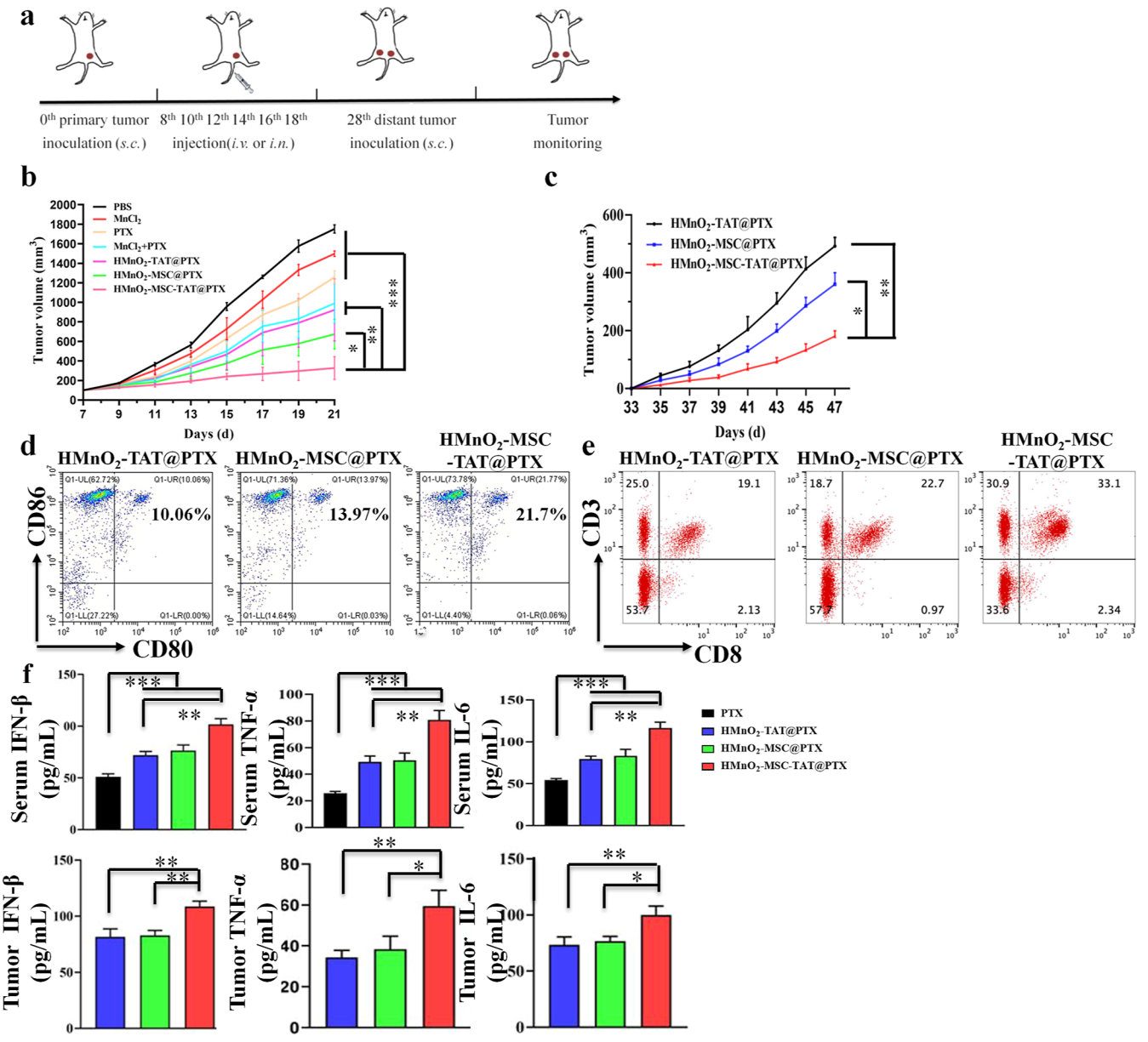

Figure 6. Inhibition of distant tumor growth by $HMnO_2$-MSC-TAT NPs. (a) Schematic illustration of $HMnO_2$-MSC-TAT NP experiment design. (b,c) LLC tumor growth curves for primary tumors (b) and distant tumors (c) in mice. Data are presented as the mean ± SD (n = 3), and statistical significance was calculated using Student's t test (*p < 0.05, **p < 0.01, and ***p < 0.001). (d,e) Percentages of mature DCs ($CD80^+CD86^+$) and CTLs ($CD3^+CD8^+$) in distant tumor. (f) Secretion of cytokines in serum and distant tumor tissues was measured by ELISA (levels of IFN-β, TNF-α, and IL-6). Significance between each pair of groups was calculated using Student's t test. *p < 0.05, **p < 0.01, and ***p < 0.001.

Moreover, $HMnO_2$-MSC-TAT@PTX significantly extended the survival time (Figure 5e). Notably, 4 out of 10 mice survived until day 55 after treatment with $HMnO_2$-MSC-TAT@PTX. As shown in the HE-stained sections (Figure S9), areas with massive apoptosis or necrosis were observed in tumor sections from mice treated with $HMnO_2$-MSC-TAT@PTX. These results strongly demonstrate that the direct intranuclear delivery of PTX by $HMnO_2$-MSC-TAT induced a substantially stronger tumor inhibition than other delivery systems.

Inhibition of Distant Tumor Growth by Various Treatments In Vivo. To determine whether such a $HMnO_2$-MSC-TAT@PTX would inhibit the relapse and metastasis of tumors, a bilateral lung tumor model mimicking relapse and metastasis was established (Figure 6a). Lewis lung cells (LLCs) (tumor cells) were subcutaneously injected into both the right (primary tumor) and left (distant tumor) inguinal regions of the mice. Consistent with the results described above (Figure 5b), the $HMnO_2$-MSC-TAT effectively inhibited the primary tumor progression compared with other groups (Figures 6b and S10). Before the end of the observation period, the mice of non-NP groups (PBS, $MnCl_2$, free PTX, and $MnCl_2$ + PTX) had to be euthanized as the primary tumor volume exceeded 2000 mm^3. Notably, the growth of the right-side tumors (distant tumors) in the $HMnO_2$-TAT@PTX NP, $HMnO_2$-MSC-TAT@PTX NP, and $HMnO_2$-MSC-TAT@PTX NP groups was significantly inhibited (Figure 6c). This may be attributed to the activation of

https://doi.org/10.1021/acsami.3c01176
ACS Appl. Mater. Interfaces 2023, 15, 10541−10553

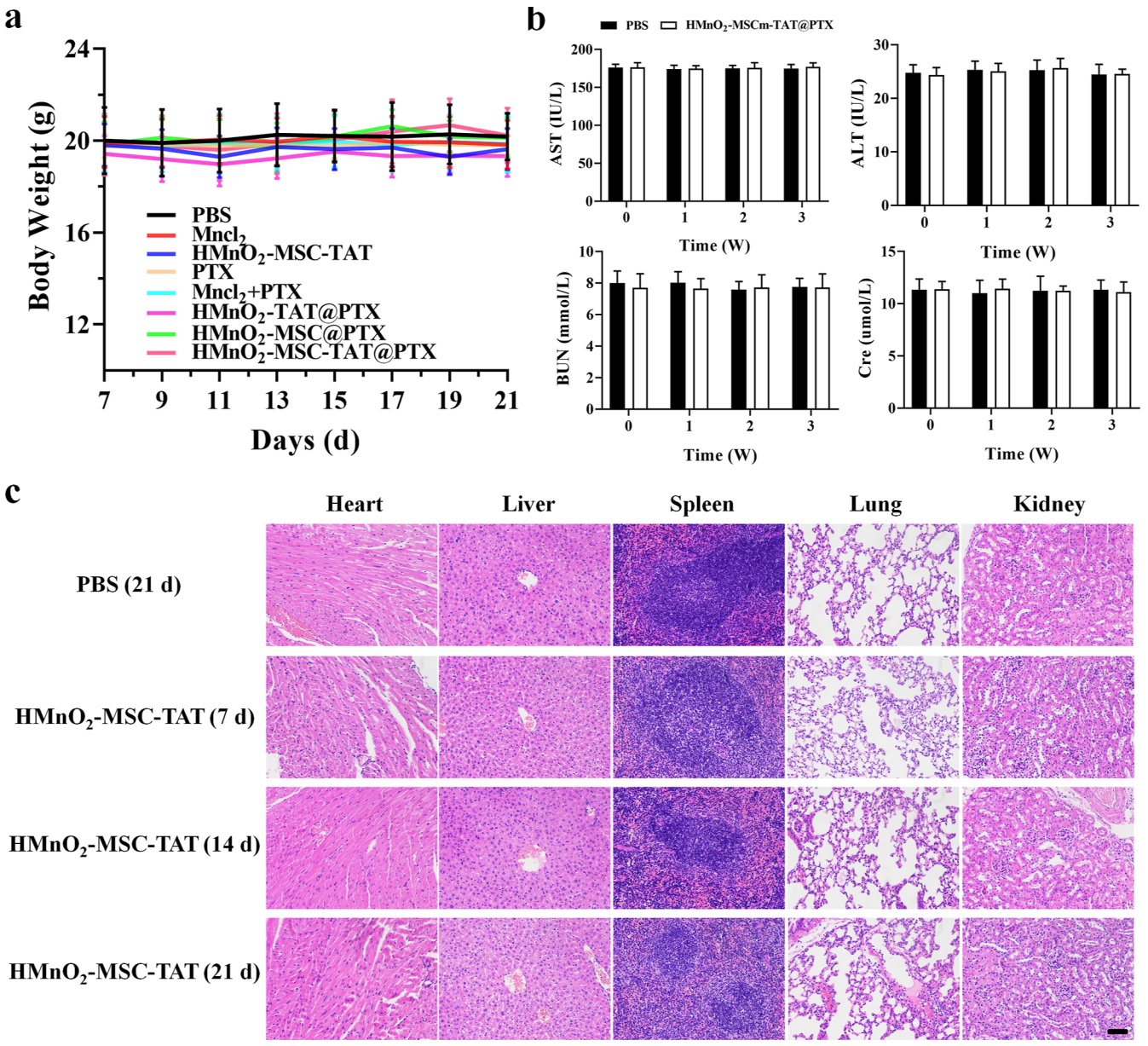

Figure 7. Biosafety of $HMnO_2$-MSC-TAT NPs. (a) Body weight of tumor-bearing mice was monitored during the treatment period (15 days). Data are presented as the mean ± SD (n = 4). (b) Serum levels of biochemical parameters, including AST, ALT, Cre, and BUN, in mice at various time points after treatment with $HMnO_2$-MSC-TAT NPs. Data are presented as the mean ± SD (n = 3). (c) HE staining of mouse organs at various time points after treatment with $HMnO_2$-MSC-TAT NPs. The scale bar is 50 μm.

cGAS/STING pathways and promotion of DC maturation by the treatment of primary tumor with $HMnO_2$-MSC-TAT@PTX, which significantly induced CTLs to kill the metastatic tumors cells. As shown in Figure 6d,e, the $HMnO_2$-MSC-TAT@PTX-treated group showed the largest number of mature DCs and CTLs at the distant tumor regions, suggesting that it could induce systemic immune responses.

Secretion of cytokines, such as IFN-β, TNF-α, and IL-6 which are critical immunostimulatory cytokines and are important for the formation of antitumor immune responses, was measured.[44] As shown in Figure 6f, $HMnO_2$-MSC-TAT@PTX induced the highest levels of IFN-β, TNF-α, and IL-6 in serum and distant tumors compared to $HMnO_2$-TAT@PTX and $HMnO_2$-MSC@PTX. The above observations unambiguously demonstrated that $HMnO_2$-MSC-TAT@PTX boosted systemic immune responses to inhibit tumor relapse and metastasis.

Safety Evaluation of $HMnO_2$-MSC-TAT@PTX In Vivo. In addition to the therapeutic efficacy, safety is also crucial for applications in the clinic. The body weights had no obvious changes in the treated mice (Figure 7a), suggesting that $HMnO_2$-MSC-TAT@PTX has no systemic toxicity. Compared with PBS control, the levels of aspartate aminotransferase (AST), alanine aminotransferase (ALT), creatinine (Cre), and blood urea nitrogen (BUN) in mice receiving nano-carriers treatment showed no significant elevation (Figure 7b). In addition, H&E staining showed that there were no obvious inflammatory infiltrates or morphological differences of the major organs compared with control (Figure 7c). These results proved the safety of $HMnO_2$-MSC-TAT@PTX NPs in vivo.

https://doi.org/10.1021/acsami.3c01176
ACS Appl. Mater. Interfaces 2023, 15, 10541−10553

CONCLUSIONS

In summary, a potent biomimetic nanoplatform consisting of an $HMnO_2$ NP core and human umbilical cord-derived MSC membrane surface cloaking with TAT peptide modification was developed for the systemic treatment of NSCLC. The nanocarriers could be taken up by tumor cells, penetrate into nuclei, release the drug, and eliminate tumor cells. Furthermore, the NPs achieved targeted delivery of chemotherapeutic drugs into the cancer cell nuclei and induced the maturation of DCs and infiltration of T cells, resulting in efficient inhibition of the growth, relapse, and metastasis of tumors. Direct intranuclear delivery of chemotherapeutics could be a potential approach in lung cancer therapy.

METHODS

Cell Line and Animal. LLCs, LO2 cells, BEAS-2B cells, and A549 cells were grown in Dulbecco's modified Eagle's medium supplemented with 10% fetal bovine serum and 1% 100 U/mL penicillin/streptomycin at 37 °C under 5% CO_2. WT C57BL/6 mice (6−8 weeks) and BALB/c nude mice were housed under normal conditions. All animal experiments were performed with the approval of the Nanjing Medical University Laboratory Animal Center (Jiangsu, China).

Synthesis of $HMnO_2$ NPs. Hollow manganese dioxide ($HMnO_2$) NPs were synthesized following the reported method.[37] First, solid silica NPs ($sSiO_2$) were prepared by the widely adopted Stöber method.[38] Then, 25 mL of absolute ethanol, 0.5 mL of distilled water, and 1.5 mL of aqueous ammonia were mixed in a flask while stirring at 500 rpm for 10 min. Then, 0.75 mL of TEOS was added dropwise while stirring at 40 °C, and the reaction proceeded for 12 h. Next, $sSiO_2$ was obtained by centrifugation at 10,000 rpm for 20 min and washed with absolute ethanol and distilled water three times.

Second, the synthesized Stöber NPs were coated with a mesoporous manganese dioxide shell. For this step, the obtained $sSiO_2$ (20 mg) was redispersed in distilled water, and then, $KMnO_4$ solution (150 mg) was added drop by drop into the above solution at room temperature while stirring at 500 rpm for 6 h. Next, the mesoporous MnO_2-coated $sSiO_2$ NPs (SiO_2@MnO_2) were precipitated by centrifugation at 15,000 rpm for 20 min and washed with distilled water three times.

Third, $HMnO_2$ NPs were formed by etching with sodium carbonate. The as-synthesized mesoporous SiO_2@MnO_2 was added to 2 M sodium carbonate aqueous solution at 60 °C, and the reaction proceeded for 12 h. The product was centrifuged and washed thrice with distilled water.

Preparation of $HMnO_2$-MSC-TAT@PTX NPs. For loading PTX, the $HMnO_2$ solution (0.2 mg/mL) was incubated with various concentrations of PTX for 24 h at room temperature to form $HMnO_2$@PTX NPs.

The human umbilical cord mesenchymal stem cell membrane was prepared using the reported method.[22] The resulting packed MSC membranes were obtained by differential centrifugation and resuspended in 1× PBS. Then, membrane fragments were coextruded with $HMnO_2$@PTX nanoparticulate cores to form MSC membrane-coated NPs and then dispersed in PBS. To form TAT peptide-modified MSC membranes, 0.1 mg/mL DSPE-PEG-TAT was added to the above solution while stirring for 2 h, and DSPE-PEG-TAT was inserted into the MSC membranes using a lipid-insertion approach.[39] Next, the mixture was redispersed in PBS buffer.

Preparation of $HMnO_2$-TAT@PTX NPs. The $HMnO_2$ NPs were synthesized, as described above. Then, 5 mL of $HMnO_2$ solution (2 mg/mL) was mixed with 10 mL of PAH solution (5 mg/mL) and ultrasonicated for 2 h, and the precipitate was washed with distilled water three times. The solution of $HMnO_2$/PAH was mixed with 10 mL of PAA (5 mg/mL) and ultrasonicated for 2 h, and $HMnO_2$/PAH/PAA was collected by centrifugation and washed with water three times. The obtained $HMnO_2$/PAH/PAA was mixed with 50 mg of NH_2-PEG-NH_2 and ultrasonicated for 1 h. TAT was dissolved with 1-ethyl-3-(3-dimethly_aminopropyl) carbodiimide (EDC) and N-hydroxysuccinimide (NHS), and the mixture was stirred for 30 min. Then, $HMnO_2$−NH_2 was added to the above solution, and the mixture was stirred for 12 h. The prepared $HMnO_2$-TAT was collected by repeatedly washing the NPs. For PTX loading, the $HMnO_2$-TAT solution (0.2 mg/mL) was added to various concentrations of PTX for 24 h. The $HMnO_2$-TAT@PTX was obtained by centrifugation and washed with water three times.

Characterization of NPs. The hydrodynamic diameters and zeta potentials of the NPs were determined by DLS (Malvern Instruments, UK). The morphology of $HMnO_2$-MSC-TAT NPs was characterized by TEM (FEI Tecnai G2, USA) and SEM (Zeiss Sigma 300, Germany). UV−vis spectra were measured using a PerkinElmer Lambda 750 UV−vis−NIR spectrophotometer. The surface area and pore size of $HMnO_2$ were measured by a Surface Area and Porosity Analyzer (ASAP2460, USA). The concentrations of Mn were determined by ICP-OES (ICPE 9000, Japan). The protein contents in the membranes of the NPs were measured by SDS-PAGE.

Biocompatibility. LO2 cells and BEAS-2B cells were used for biocompatibility studies. Cells in 0.2 mL of cell culture medium were incubated with various concentrations of $HMnO_2$-MSC-TAT (3.13, 6.25, 12.5, 25, 50, 100, and 200 μg/mL) for 24 h. Cell viability was assessed by the standard MTT assay.

In Vitro Encapsulation and Loading of PTX. The PTX content in $HMnO_2$-MSC-TAT@PTX NPs and $HMnO_2$-MSC-TAT@PTX NPs was measured by an UV−vis spectrometer at 227 nm. The drug loading efficiency and encapsulation efficiency were calculated as follows

$$\text{loading efficiency}(\%) = (\text{the total weight of PTX} - \text{the weight of free drug})/\text{total weight of NPs} \times 100\%$$

$$\text{encapsulation efficiency}(\%) = (\text{the total weight of PTX} - \text{the weight of free drug})/\text{initial weight of PTX} \times 100\%$$

In Vitro Degradation and Release of PTX. $HMnO_2$ was incubated in PBS at different pH values (5.5, 6.5, and 7.4) for various durations, and the solution was characterized by TEM and UV−vis spectrometry. The release of PTX from NPs was measured by dialysis against PBS with different pH values (5.5 and 7.4) at 37 °C. The level of PTX release at predetermined time intervals (30 min, 45 min, 1 h, 2 h, 4 h, 8 h, 12 h, and 24 h) was determined by the UV−vis spectra.

In Vitro Cell Uptake. A549 cells were seeded and cultured for 24 h at 37 °C. Cell were incubated with fluorescently labeled NPs ($HMnO_2$-TAT@FITC, $HMnO_2$-MSC@FITC, and $HMnO_2$-MSC-TAT@FITC) for 12 h. After incubation, the cells were washed with PBS and fixed with 4% cold paraformaldehyde for 15 min. Then, the cells were stained with DAPI for 15 min and observed by CLSM (Lsm710, Germany).

In Vitro Quantification of NPs in the Cells and in the Nucleus. A549 cells at a density of 3×10^6 cells were treated with $HMnO_2$-TAT, $HMnO_2$-MSC, or $HMnO_2$-MSC-TAT (100 μg/mL) for 4, 12, and 24 h. Cell nuclei were isolated from the cytosol according to a reported method.[38] The cells were suspended in a 100 mM NaCl solution with 1 mM EDTA, 1% Triton X-100, and 10 mM Tris buffer (pH 7.4). Then, the suspension was centrifuged, and the precipitate of cell nuclei was obtained. Next, 3 mL of cell lysis solution was added to disrupt the cell nuclei. The mass of $HMnO_2$-TAT, $HMnO_2$-MSC, or $HMnO_2$-MSC-TAT in the A549 cell nuclei was assessed by measuring the Mn concentration with ICP-OES. The cellular uptake of $HMnO_2$-TAT, $HMnO_2$-MSC, or $HMnO_2$-MSC-TAT was measured, as described above without the step of nuclei isolation.

In Vitro Cytotoxicity and Apoptosis Tests. The cytotoxicity of $HMnO_2$-TAT, $HMnO_2$-MSC, or $HMnO_2$-MSC-TAT was determined by MTT assay. A549 cells were incubated with various concentrations

https://doi.org/10.1021/acsami.3c01176
ACS Appl. Mater. Interfaces 2023, 15, 10541−10553

of NPs (3.13, 6.25, 12.5, 25, 50, 100, and 200 μg/mL) for 24 h. Relative cell viability was calculated as the percentage in relation to untreated control cells. The therapeutic effect of NPs loaded with PTX was assessed, as described above.

For flow cytometric analysis, A549 cells at a density of 5×10^5 cells were treated with free PTX, $HMnO_2$-TAT@PTX, $HMnO_2$-MSC@PTX, or $HMnO_2$-MSC-TAT@PTX NPs for 24 h in a six-well plate. Then, cancer cells were stained with Annexin-V-FITC and propidium iodide (PI) and analyzed by flow cytometry (BD FACSCalibur, USA).

In Vivo Fluorescence Imaging. BALB/c nude mice were injected with 1×10^5 A549 cells in the right flank. ICG, a near-infrared fluorescent dye, was used to label the NPs. Free ICG, $HMnO_2$-TAT@ICG, $HMnO_2$-MSC@ICG, or $HMnO_2$-MSC-TAT@ICG were injected intravenously. Fluorescence images were captured at different time points (1, 2, 6, 8, 12, and 24 h) postinjection using a Lumina LT Series III (PerkinElmer, USA).

In Vivo Pharmacokinetics and Biodistribution. Female C57BL/6 mice were injected subcutaneously with 1×10^5 LLC cells on the right flank. Free PTX, $HMnO_2$-TAT@PTX, $HMnO_2$-MSC@PTX, or $HMnO_2$-MSC-TAT@PTX (PTX: 4 mg/kg) were injected into the tail vein of tumor-bearing mice. Eye arterial blood was withdrawn at designated times (0.5, 1, 2, 4, 8, 12, 24, 36, and 48 h) after drug injection. After centrifugation at 5000 rpm for 8 min, 100 μL of plasma was maintained at −20 °C. Then, PTX was extracted by vortexing with chloroform/methanol for 5 min and centrifuged at 15,000 rpm for 5 min to collect the lower solution for detection. The collected solution was dried under nitrogen and dissolved in methanol before it was analyzed by HPLC (LC-10AT, Japan).

For biodistribution, the heart, liver, spleen, lung, kidney, and tumor were collected at 24 h after injection. The tissues were then washed with saline, weighed, and homogenized. The PTX content was quantified by the HPLC method mentioned above.

In Vivo Therapeutic Efficacy. Female C57BL/6 mice were subcutaneously injected with LLC cells (1×10^5) on the right flank (primary tumor) and the left flank (distant tumor). When tumors reached ~100 mm^3, mice were randomly divided into eight treatment groups as follows: PBS, $MnCl_2$ (5 mg/kg), $HMnO_2$-MSC-TAT (dose of MnO_2 = 5 mg/kg), free PTX (10 mg/kg), $MnCl_2$ (5 mg/kg) + free PTX (10 mg/kg), $HMnO_2$-TAT@PTX, $HMnO_2$-MSC@PTX, and $HMnO_2$-MSC-TAT@PTX (dose of MnO_2 = 5 mg/kg, PTX = 4 mg/kg). Except for the $MnCl_2$ group, all treatments were administered by i.v. injection. $MnCl_2$ was administered intranasally. The injection was performed six times every 2 days. Tumor growth and body weight of the mice were monitored every other day. The tumor volume was calculated based on the formula: volume = $width^2 \times length/2$. The mice were euthanized at the end of the study. The tissue and tumors were collected and stained by HE. Finally, the survival time of the mice was determined.

Immune Cell Infiltration in the Tumor Microenvironment. To evaluate the systemic immune responses of $HMnO_2$-MSC-TAT@PTX in tumor-bearing mice, the percentage of mature DC ($CD80^+CD86^+$) and CTLs ($CD3^+CD8^+$) in distant tumor were determined by flow cytometry. The single-cell suspensions were harvested by digestion of tumor tissue. For mature DC evaluation, cells were stained with anti-CD80 and anti-CD86 monoclonal antibodies. Meanwhile, cells were stained with anti-CD3 and anti-CD8 monoclonal antibodies for evaluating CTL infiltration.

ELISA. The HMGB1 concentration in the cell supernatant was detected by an HMGB1 ELISA kit according to manufacturer's instruction. Interferon-beta (IFN-β), tumor necrosis factor alpha (TNF-α), and interleukin-6 (IL-6) in the blood samples and tumor samples of mice were measured by ELISA.

Statistical Analysis. Data are expressed as the mean ± standard deviation (SD) and estimated by the analysis of Student's t test or one-way analysis of variance. Differences were considered statistically significant at $^*p < 0.05$, $^{**}p < 0.01$, and $^{***}p < 0.001$.

■ ASSOCIATED CONTENT

Supporting Information

The Supporting Information is available free of charge at https://pubs.acs.org/doi/10.1021/acsami.3c01176.

TEM images of SiO_2 NPs, SiO_2@MnO_2 NPs, and $HMnO_2$ NPs; SEM image of $HMnO_2$ NPs; UV−vis spectra of TAT peptide; $HMnO_2$ NPs and $HMnO_2$-MSC-TAT NPs; characterization of $HMnO_2$-TAT NPs; cytotoxicity of $HMnO_2$-MSC-TAT NPs to LO2 and BEAS-2B cells; degradation behavior of $HMnO_2$-MSC-TAT NPs; N_2 adsorption/desorption isotherms and pore size distribution curves of the $HMnO_2$ NPs; cytotoxicity of $HMnO_2$-TAT NPs, $HMnO_2$-MSC NPs, and $HMnO_2$-MSC-TAT NPs to A549 cells; HE staining of tumor tissues after different treatments; and representative images of the excised tumors after different treatments (PDF)

■ AUTHOR INFORMATION

Corresponding Author

Ganzhu Feng − *Department of Respiratory and Critical Care Medicine, The Second Affiliated Hospital of Nanjing Medical University, Nanjing, Jiangsu 211000, China;* orcid.org/0000-0003-3926-1753; Email: zhu1635253@163.com

Authors

Lixu Xie − *Department of Respiratory and Critical Care Medicine, The Second Affiliated Hospital of Nanjing Medical University, Nanjing, Jiangsu 211000, China; Department of Respiratory and Critical Care Medicine, Qilu Hospital of Shandong University, Jinan, Shandong 250012, China;* orcid.org/0000-0003-1189-6618

Changwen Zhang − *Department of Respiratory and Critical Care Medicine, The Second Affiliated Hospital of Nanjing Medical University, Nanjing, Jiangsu 211000, China*

Miao Liu − *Department of Pediatrics, Qingyun County People's Hospital, Dezhou 253700, China*

Jianling Huang − *Department of Respiratory and Critical Care Medicine, The Second Affiliated Hospital of Nanjing Medical University, Nanjing, Jiangsu 211000, China*

Xiao Jin − *Department of Respiratory and Critical Care Medicine, The Second Affiliated Hospital of Nanjing Medical University, Nanjing, Jiangsu 211000, China*

Changjun Zhu − *Department of Respiratory and Critical Care Medicine, The Second Affiliated Hospital of Nanjing Medical University, Nanjing, Jiangsu 211000, China*

Minjie Lv − *Department of Respiratory and Critical Care Medicine, The Second Affiliated Hospital of Nanjing Medical University, Nanjing, Jiangsu 211000, China*

Ning Yang − *Department of Respiratory and Critical Care Medicine, The Second Affiliated Hospital of Nanjing Medical University, Nanjing, Jiangsu 211000, China*

Sixi Chen − *Department of Respiratory and Critical Care Medicine, The Second Affiliated Hospital of Nanjing Medical University, Nanjing, Jiangsu 211000, China*

Mingyue Shao − *Department of Respiratory and Critical Care Medicine, The Second Affiliated Hospital of Nanjing Medical University, Nanjing, Jiangsu 211000, China*

Xingran Du − *Department of Infectious Disease, The Second Affiliated Hospital of Nanjing Medical University, Nanjing, Jiangsu 211000, China*

Complete contact information is available at:

https://pubs.acs.org/10.1021/acsami.3c01176

Notes

The authors declare no competing financial interest.

■ ACKNOWLEDGMENTS

G.F. received funding from the National Natural Science Foundation of China (no. 82070017 and 81870009). We appreciate suggestions from Yue Wang of China Pharmaceutical University.

■ REFERENCES

(1) Sung, H.; Ferlay, J.; Siegel, R. L.; Laversanne, M.; Soerjomataram, I.; Jemal, A.; Bray, F. Global Cancer Statistics 2020: GLOBOCAN Estimates of Incidence and Mortality Worldwide for 36 Cancers in 185 Countries. *Ca-Cancer J. Clin.* **2021**, *71*, 209−249.

(2) Allemani, C.; Matsuda, T.; Di Carlo, V.; Harewood, R.; Matz, M.; Nikšić, M.; Bonaventure, A.; Valkov, M.; Johnson, C. J.; Estève, J.; Ogunbiyi, O. J.; Azevedo E Silva, G.; Chen, W. Q.; Eser, S.; Engholm, G.; Stiller, C. A.; Monnereau, A.; Woods, R. R.; Visser, O.; Lim, G. H.; Aitken, J.; Weir, H. K.; Coleman, M. P.; CONCORD Working Group. Global Surveillance of Trends in Cancer Survival 2000-14 (CONCORD-3): Analysis of Individual Records for 37513025 Patients Diagnosed with one of 18 Cancers from 322 Population-Based Registries in 71 Countries. *Lancet* **2018**, *391*, 1023−1075.

(3) Huang, L.; Cronin, K. A.; Johnson, K. A.; Mariotto, A. B.; Feuer, E. J. Improved Survival Time: What Can Survival Cure Models Tell Us about Population-Based Survival Improvements in Late-Stage Colorectal, Ovarian, and Testicular Cancer? *Cancer* **2008**, *112*, 2289−2300.

(4) Wu, T.; Dai, Y. Tumor Microenvironment and Therapeutic Response. *Cancer Lett.* **2017**, *387*, 61−68.

(5) Ji, T.; Zhao, Y.; Ding, Y.; Nie, G. Using Functional Nanomaterials to Target and Regulate the Tumor Microenvironment: Diagnostic and Therapeutic Applications. *Adv. Mater.* **2013**, *25*, 3508−3525.

(6) Xu, P.; Meng, Q.; Sun, H.; Yin, Q.; Yu, H.; Zhang, Z.; Cao, M.; Zhang, Y.; Li, Y. Shrapnel Nanoparticles Loading Docetaxel Inhibit Metastasis and Growth of Breast Cancer. *Biomaterials* **2015**, *64*, 10−20.

(7) Yu, M. K.; Park, J.; Jon, S. Targeting Strategies for Multifunctional Nanoparticles in Cancer Imaging and Therapy. *Theranostics* **2012**, *2*, 3−44.

(8) Yao, S.; Li, L.; Su, X. T.; Wang, K.; Lu, Z. J.; Yuan, C. Z.; Feng, J. B.; Yan, S.; Kong, B. H.; Song, K. Development and Evaluation of Novel Tumor-Targeting Paclitaxel-Loaded Nanocarriers for Ovarian Cancer Treatment: in Vitro and in Vivo. *J. Exp. Clin. Cancer Res.* **2018**, *37*, 29.

(9) Ji, T.; Ding, Y.; Zhao, Y.; Wang, J.; Qin, H.; Liu, X.; Lang, J.; Zhao, R.; Zhang, Y.; Shi, J.; Tao, N.; Qin, Z.; Nie, G. Peptide Assembly Integration of Fibroblast-Targeting and Cell-Penetration Features for Enhanced Antitumor Drug Delivery. *Adv. Mater.* **2015**, *27*, 1865−1873.

(10) Chen, F.; Hong, H.; Zhang, Y.; Valdovinos, H. F.; Shi, S.; Kwon, G. S.; Theuer, C. P.; Barnhart, T. E.; Cai, W. In Vivo Tumor Targeting and Image-Guided Drug Delivery with Antibody-Conjugated, Radiolabeled Mesoporous Silica Nanoparticles. *ACS Nano* **2013**, *7*, 9027−9039.

(11) Nie, S. M. Understanding and Overcoming Major Barriers in Cancer Nanomedicine. *Nanomedicine* **2010**, *5*, 523−528.

(12) Hu, C.; Fang, R.; Zhang, L. Erythrocyte-Inspired Delivery Systems. *Adv. Healthcare Mater.* **2012**, *1*, 537−547.

(13) Palucka, K.; Banchereau, J. Cancer Immunotherapy via Dendritic Cells. *Nat. Rev. Cancer* **2012**, *12*, 265−277.

(14) Kang, S.; Bhang, S. H.; Hwang, S.; Yoon, J. K.; Song, J.; Jang, H. K.; Kim, S.; Kim, B. S. Mesenchymal Stem Cells Aggregate and Deliver Gold Nanoparticles to Tumors for Photothermal Therapy. *ACS Nano* **2015**, *9*, 9678−9690.

(15) Madsen, S. J.; Baek, S. K.; Makkouk, A. R.; Krasieva, T.; Hirschberg, H. Macrophages as Cell-Based Delivery Systems for Nanoshells in Photothermal Therapy. *Ann. Biomed. Eng.* **2012**, *40*, 507−515.

(16) Huang, X.; Zhang, F.; Wang, H.; Niu, G.; Choi, K. Y.; Swierczewska, M.; Zhang, G.; Gao, H.; Wang, Z.; Zhu, L.; Choi, H. S.; Lee, S.; Chen, X. Mesenchymal Stem Cell-Based Cell Engineering with Multifunctional Mesoporous Silica Nanoparticles for Tumor Delivery. *Biomaterials* **2013**, *34*, 1772−1780.

(17) Gao, C.; Lin, Z.; Wu, Z.; Lin, X.; He, Q. Stem-Cell-Membrane Camouflaging on Near-Infrared Photoactivated Upconversion Nanoarchitectures for in Vivo Remote-Controlled Photodynamic Therapy. *ACS Appl. Mater. Interfaces* **2016**, *8*, 34252−34260.

(18) Ma, F.; Chen, D.; Chen, F.; Chi, Y.; Han, Z.; Feng, X.; Li, X.; Han, Z. Human Umbilical Cord Mesenchymal Stem Cells Promote Breast Cancer Metastasis by Interleukin-8- and Interleukin-6-Dependent Induction of CD44 (+)/CD24 (-) Cells. *Cell Transplant.* **2015**, *24*, 2585−2599.

(19) Li, H. J.; Reinhardt, F.; Herschman, H. R.; Weinberg, R. A. Cancer-Stimulated Mesenchymal Stem Cells Create a Carcinoma Stem Cell Niche via Prostaglandin E2 Signaling. *Cancer Discov.* **2012**, *2*, 840−855.

(20) Huang, W. H.; Chang, M. C.; Tsai, K. S.; Hung, M. C.; Chen, H. L.; Hung, S. C. Mesenchymal Stem Cells Promote Growth and Angiogenesis of Tumors in Mice. *Oncogene* **2013**, *32*, 4343−4354.

(21) Wei, X.; Yang, X.; Han, Z. P.; Qu, F. F.; Shao, L.; Shi, Y. F. Mesenchymal Stem Cells: A New Trend for Cell Therapy. *Acta Pharmacol. Sin.* **2013**, *34*, 747−754.

(22) Hu, C. M.; Zhang, L.; Aryal, S.; Cheung, C.; Fang, R. H.; Zhang, L. Erythrocyte Membrane-Camouflaged Polymeric Nanoparticles as a Biomimetic Delivery Platform. *Proc. Natl. Acad. Sci. U.S.A.* **2011**, *108*, 10980−10985.

(23) Hu, C. M.; Fang, R. H.; Wang, K. C.; Luk, B. T.; Thamphiwatana, S.; Dehaini, D.; Nguyen, P.; Angsantikul, P.; Wen, C. H.; Kroll, A. V.; Carpenter, C.; Ramesh, M.; Qu, V.; Patel, S. H.; Zhu, J.; Shi, W.; Hofman, F. M.; Chen, T. C.; Gao, W.; Zhang, K.; Chien, S.; Zhang, L. Nanoparticle Biointerfacing by Platelet Membrane Cloaking. *Nature* **2015**, *526*, 118−121.

(24) Kroll, A. V.; Fang, R. H.; Zhang, L. F. Biointerfacing and Applications of Cell Membrane-Coated Nanoparticles. *Bioconjugate Chem.* **2017**, *28*, 23−32.

(25) Rao, L.; Meng, Q. F.; Huang, Q.; Liu, P.; Bu, L. L.; Kondamareddy, K. K.; Guo, S. S.; Liu, W.; Zhao, X. Z. Photocatalytic Degradation of Cell Membrane Coatings for Controlled Drug Release. *Adv. Healthcare Mater.* **2016**, *5*, 1420−1427.

(26) Su, J.; Sun, H.; Meng, Q.; Zhang, P.; Yin, Q.; Li, Y. Enhanced Blood Suspensibility and Laser-Activated Tumor-Specific Drug Release of Theranostic Mesoporous Silica Nanoparticles by Functionalizing with Erythrocyte Membranes. *Theranostics* **2017**, *7*, 523−537.

(27) Krishnamurthy, S.; Gnanasammandhan, M. K.; Xie, C.; Huang, K.; Cui, M. Y.; Chan, J. M. Monocyte Cell Membrane-Derived Nanoghosts for Targeted Cancer Therapy. *Nanoscale* **2016**, *8*, 6981−6985.

(28) Cao, H.; Dan, Z.; He, X.; Zhang, Z.; Yu, H.; Yin, Q.; Li, Y. Liposomes Coated with Isolated Macrophage Membrane Can Target Lung Metastasis of Breast Cancer. *ACS Nano* **2016**, *10*, 7738−7748.

(29) Tang, J.; Shen, D.; Caranasos, T. G.; Wang, Z.; Vandergriff, A. C.; Allen, T. A.; Hensley, M. T.; Dinh, P. U.; Cores, J.; Li, T. S.; Zhang, J.; Kan, Q.; Cheng, K. Therapeutic Microparticles Functionalized with Biomimetic Cardiac Stem Cell Membranes and Secretome. *Nat. Commun.* **2017**, *8*, 13724.

(30) Gao, C.; Lin, Z.; Jurado-Sánchez, B.; Lin, X.; Wu, Z.; He, Q. Stem Cell Membrane-Coated Nanogels for Highly Efficient in Vivo Tumor Targeted Drug Delivery. *Small* **2016**, *12*, 4056−4062.

(31) Hu, Q.; Qian, C.; Sun, W.; Wang, J.; Chen, Z.; Bomba, H. N.; Xin, H.; Shen, Q.; Gu, Z. Engineered Nanoplatelets for Enhanced

Treatment of Multiple Myeloma and Thrombus. *Adv. Mater.* **2016**, *28*, 9573−9580.
(32) Li, J.; Ai, Y.; Wang, L.; Bu, P.; Sharkey, C. C.; Wu, Q.; Wun, B.; Roy, S.; Shen, X.; King, M. R. Targeted Drug Delivery to Circulating Tumor Cells via Platelet Membrane-Functionalized Particles. *Biomaterials* **2016**, *76*, 52−65.
(33) Yang, N.; Ding, Y.; Zhang, Y.; Wang, B.; Zhao, X.; Cheng, K.; Huang, Y.; Taleb, M.; Zhao, J.; Dong, W. F.; Zhang, L.; Nie, G. Surface Functionalization of Polymeric Nanoparticles with Umbilical Cord-Derived Mesenchymal Stem Cell Membrane for Tumor-Targeted Therapy. *ACS Appl. Mater. Interfaces* **2018**, *10*, 22963−22973.
(34) Pan, L. M.; Liu, J. N.; Shi, J. L. Cancer Cell Nucleus-Targeting Nanocomposites for Advanced Tumor Therapeutics. *Chem. Soc. Rev.* **2018**, *47*, 6930−6946.
(35) Chen, P.; Luo, S.; Wen, Y. J.; Li, Y. H.; Li, J.; Wang, Y. S.; Du, L. C.; Zhang, P.; Tang, J.; Yang, D. B.; Hu, H. Z.; Zhao, X.; Wei, Y. Q. Low-Dose Paclitaxel Improves the Therapeutic Efficacy of Recombinant Adenovirus Encoding CCL21 Chemokine Against Murine Cancer. *Cancer Sci.* **2014**, *105*, 1393−1401.
(36) Lv, M.; Chen, M.; Zhang, R.; Zhang, W.; Wang, C.; Zhang, Y.; Wei, X.; Guan, Y.; Liu, J.; Feng, K.; Jing, M.; Wang, X.; Liu, Y. C.; Mei, Q.; Han, W.; Jiang, Z. Manganese is Critical for Antitumor Immune Responses via cGAS-STING and Improves the Efficacy of Clinical Immunotherapy. *Cell Res.* **2020**, *30*, 966−979.
(37) Yang, G.; Xu, L.; Chao, Y.; Xu, J.; Sun, X.; Wu, Y.; Peng, R.; Liu, Z. Hollow MnO_2 as a Tumor-Microenvironment-Responsive Biodegradable Nano-Platform for Combination Therapy Favoring Antitumor Immune Responses. *Nat. Commun.* **2017**, *8*, 902.
(38) Stöber, W.; Fink, A.; Bohn, E. Controlled Growth of Monodisperse Silica Spheres in Micron Size Range. *J. Colloid Interface Sci.* **1968**, *26*, 62−69.
(39) Fang, R. H.; Hu, C. M.; Chen, K. N.; Luk, B. T.; Carpenter, C. W.; Gao, W.; Li, S.; Zhang, D. E.; Lu, W.; Zhang, L. Lipid-Insertion Enables Targeting Functionalization of Erythrocyte Membrane-Cloaked Nanoparticles. *Nanoscale* **2013**, *5*, 8884−8888.
(40) Song, Q.; Yin, Y.; Shang, L.; Wu, T.; Zhang, D.; Kong, M.; Zhao, Y.; He, Y.; Tan, S.; Guo, Y.; Zhang, Z. Tumor Microenvironment Responsive Nanogel for the Combinatorial Antitumor Effect of Chemotherapy and Immunotherapy. *Nano Lett.* **2017**, *17*, 6366−6375.
(41) Lau, T. S.; Chan, L. K. Y.; Man, G. C. W.; Wong, C. H.; Lee, J. H. S.; Yim, S. F.; Cheung, T. H.; McNeish, I. A.; Kwong, J. Paclitaxel Induces Immunogenic Cell Death in Ovarian Cancer via TLR4/IKK2/SNARE-Dependent Exocytosis. *Cancer Immunol. Res.* **2020**, *8*, 1099−1111.
(42) Zhou, L.; Xu, Q.; Huang, L.; Jin, J.; Zuo, X.; Zhang, Q.; Ye, L.; Zhu, S.; Zhan, P.; Ren, J.; Lv, T.; Song, Y. Low-dose carboplatin reprograms tumor immune microenvironment through STING signaling pathway and synergizes with PD-1 inhibitors in lung cancer. *Cancer Lett.* **2021**, *500*, 163−171.
(43) Hou, L.; Tian, C.; Yan, Y.; Zhang, L.; Zhang, H.; Zhang, Z. Manganese-Based Nanoactivator Optimizes Cancer Immunotherapy via Enhancing Innate Immunity. *ACS Nano* **2020**, *14*, 3927−3940.
(44) Sivick, K. E.; Desbien, A. L.; Glickman, L. H.; Reiner, G. L.; Corrales, L.; Surh, N. H.; Hudson, T. E.; Vu, U. T.; Francica, B. J.; Banda, T.; Katibah, G. E.; Kanne, D. B.; Leong, J. J.; Metchette, K.; Bruml, J. R.; Ndubaku, C. O.; McKenna, J. M.; Feng, Y.; Zheng, L.; Bender, S. L.; Cho, C. Y.; Leong, M. L.; van Elsas, A.; Dubensky, T. W., Jr.; McWhirter, S. M. Magnitude of Therapeutic STING Activation Determines $CD8^+$ T Cell-Mediated Anti-Tumor Immunity. *Cell Rep.* **2018**, *25*, 3074−3085.

https://doi.org/10.1021/acsami.3c01176
ACS Appl. Mater. Interfaces 2023, 15, 10541−10553